

Origin of Fracture-Resistance to Large Volume Change in Cu-Substituted Co_3O_4 Electrodes

Heguang Liu, Qianqian Li, Zhenpeng Yao, Lei Li, Yuan Li, Chris Wolverton, Mark C. Hersam, Jinsong Wu,* and Vinayak P. Dravid*

The electrode materials conducive to conversion reactions undergo large volume change in cycles which restrict their further development. It has been demonstrated that incorporation of a third element into metal oxides can improve the cycling stability while the mechanism remains unknown. Here, an in situ and ex situ electron microscopy investigation of structural evolutions of Cu-substituted Co_3O_4 supplemented by first-principles calculations is reported to reveal the mechanism. An interconnected framework of ultrathin metallic copper formed provides a high conductivity backbone and cohesive support to accommodate the volume change and has a cube-on-cube orientation relationship with Li_2O . In charge, a portion of Cu metal is oxidized to CuO, which maintains a cube-on-cube orientation relationship with Cu. The Co metal and oxides remain as nanoclusters (less than 5 nm) thus active in subsequent cycles. This adaptive architecture accommodates the formation of Li_2O in the discharge cycle and underpins the catalytic activity of Li_2O decomposition in the charge cycle.

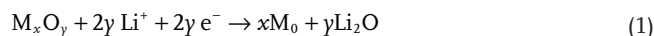
the other hand, conversion and alloying reactions occur when electrode materials, such as metal oxides,^[4] elemental Si, Sn,^[5] S,^[6] and Se^[7] are extensively lithiated and are appealing because they can involve more Li per active element, resulting in significantly higher capacities. However, unlike intercalation/deintercalation reactions, conversion and alloying reactions induce large volume changes during charge/discharge cycles that often lead to fracture and loss of electrical contact, among other deleterious mechanical effects of volume change.^[7a,8] The resulting loss of electrical contact to active electrode materials is one of the main causes of capacity loss and reduced Coulombic efficiency. In addition, most electrode materials for conversion and alloying reactions are semiconductors (and even insulators) that possess relatively low

Traditional Li-ion battery electrodes, such as graphite,^[1] Li_2MnO_4 ,^[2] and LiCoO_2 ^[3] operate by intercalation reactions alone and typically release and reaccommodate between 0.5 and 1.0 Li^+ ions per transition metal ion, thereby limiting the delivered electrode capacity to about 100–170 mA h g^{-1} . On

electronic conductivity. Thus, improved electrical conductivity would also improve the prospects of conversion and alloying reaction materials in Li-ion and related battery applications.

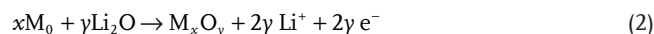
Metallic Cu is often used as the current collector at the anode in batteries due to its high electrical conductivity. Metallic Cu can also be mechanically stretched or bent significantly and repeatedly without fracture due to its high ductility and malleability. It has been demonstrated that incorporation of a third element into metal oxides/fluorides can greatly improve the cycling stability.^[9] We show here that by substituting a small amount of Cu into a Co_3O_4 lattice uniformly, the resulting composite electrode material ($\text{Cu}_{3/7}\text{Co}_{18/7}\text{O}_4$) can endure large volume change caused by lithiation/delithiation cycles, thereby maintaining high capacity and cycling stability.

The conversion/deconversion reactions between transitional metal oxides and lithium bear similarity to that in lithium–oxygen batteries, wherein Li_2O (and Li_2O_2) is repeatedly formed in the discharge cycle and decomposed in the charging cycle. The conversion reaction



is thermodynamically feasible and has a positive electromotive force.^[10] In discharge, however, large volume expansion due to Li_2O formation limits cycling stability.

The deconversion reaction



Dr. H. Liu, Dr. Q. Li, Z. Yao, Dr. L. Li, Dr. Y. Li, Prof. C. Wolverton, Prof. M. C. Hersam, Prof. J. Wu, Prof. V. P. Dravid
Department of Materials Science and Engineering
Northwestern University
Evanston, IL 60208, USA
E-mail: jinsong-wu@northwestern.edu;
v-dravid@northwestern.edu

Dr. H. Liu
School of Material Science and Engineering
Xi'an University of Technology
Xi'an 710048, China

Dr. Q. Li, Dr. Y. Li, Prof. J. Wu, Prof. V. P. Dravid
NUANCE Center
Northwestern University
Evanston, IL 60208, USA

Prof. M. C. Hersam
Department of Chemistry
and Department of Electrical Engineering and Computer Science
Northwestern University
Evanston, IL 60208, USA

 The ORCID identification number(s) for the author(s) of this article can be found under <https://doi.org/10.1002/adma.201704851>.

DOI: 10.1002/adma.201704851

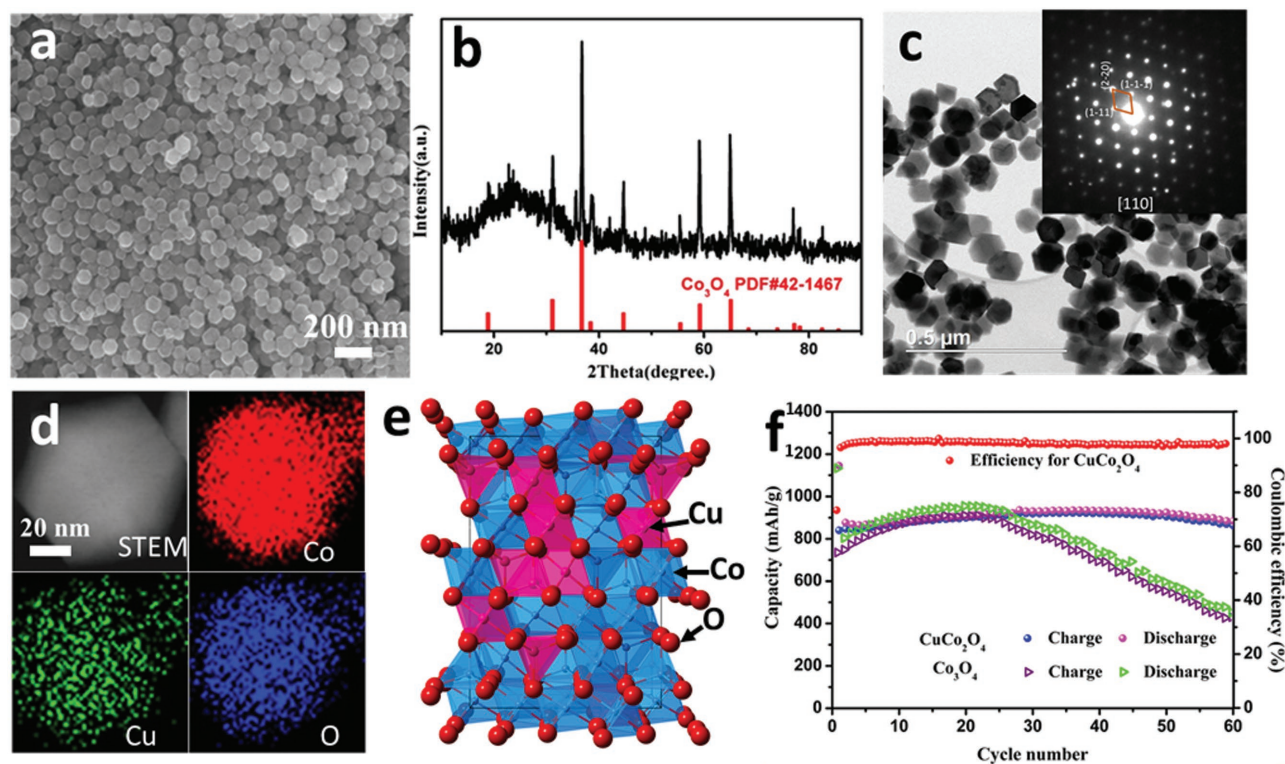


Figure 1. Cu-substituted Co_3O_4 single crystal with spinel structure, characterized by a) 20 kV SEM, b) X-ray power diffraction, c) bright-field STEM and selected area electron diffraction, and d) STEM-EDS mapping showing Co, Cu, and O maps. e) Atomic structure of nonordered $\text{Cu}_{3/7}\text{Co}_{18/7}\text{O}_4$, where Cu randomly occupies T_d or O_h sites. f) The electrochemical cycling performance of Cu-substituted Co_3O_4 and Co_3O_4 at a current density of 0.1 A g^{-1} .

involves cleavage of stable Li–O bonds, which is not a thermodynamically favorable process ($1.98 \text{ eV atom}^{-1}$). Thus, efficient decomposition of Li_2O to reduce the amount of electrochemically inactive Li_2O in the charging cycle and to keep lithium ions active in cycling are important challenges. In this work, we demonstrate Cu-substituted Co_3O_4 as a stable conversion electrode material that exhibits both high capacity and cycling stability in a single materials system.

Cu-substituted Co_3O_4 is synthesized hydrothermally, resulting in crystals as revealed by scanning electron microscope (SEM) (Figure 1a and Figure S1, Supporting Information). The crystal structure is identified to be spinel (space group: $Fd\bar{3}m$, No. 227), the same as Co_3O_4 , confirmed by both X-ray and electron diffraction (Figure 1b,c and Figure S2, Supporting Information). The elemental maps collected by X-ray energy-dispersive spectroscopy (EDS) are shown in Figure 1d. The cation ratios (Cu and Co) were varied from one sample to the other around 1:6 (as listed in Table S2, Supporting Information). The phase analyses corroborate with the nominal spinel structure of Co_3O_4 , but with a shift to low angles, indicating that copper is distributed randomly and uniformly as a solid solution. The averaged lattice parameter is identified by X-ray diffraction (Figure 1b) as $a = 8.5 \text{ \AA}$.

Similar to other binary metal oxides/fluorides,^[9] the cycling stability of the Cu-substituted Co_3O_4 has been greatly improved as shown by the electrochemical measurements. Coin-cell batteries using as-prepared Cu-substituted Co_3O_4 and pure Co_3O_4 as electrodes were fabricated and evaluated for their

lithium storage properties in the potential window of 0.01–3.0 V (vs Li/Li^+) (Figure 1f and Figure S3, Supporting Information). Cu-substituted Co_3O_4 shows a high second discharge capacity of 877 mA h g^{-1} at a current density of 0.1 A g^{-1} . After 60 cycles of charging and discharging, high capacity is retained at ≈ 863 and $\approx 883 \text{ mA h g}^{-1}$, respectively. In contrast, pure bulk Co_3O_4 shows a greatly reduced capacity ($< 200 \text{ mA h g}^{-1}$) after just 20–30 cycles.^[11] Nanosizing is an effect approach to improve the cyclability. We have measured the electrochemical properties of pure Co_3O_4 nanoparticles that are $\approx 50 \text{ nm}$ in size (Figure 1f and Figure S3, Supporting Information), which shows discharge capacity of 796 mA h g^{-1} at the second cycle. After 60 cycles at the same current density, it exhibits notably fast capacity decay, with charge and discharge capacity of 423 and 445 mA h g^{-1} , respectively. Evidently, the pure Co_3O_4 control sample exhibits significantly inferior cycling stability compared to Cu-substituted Co_3O_4 . In addition, Cu-substituted Co_3O_4 shows improved charge/discharge kinetics compared to Co_3O_4 . Figure S3d (Supporting Information) shows the capacity of Cu-substituted Co_3O_4 compared to Co_3O_4 control samples at various cycling rates ranging from 0.1 to 1.0 A g^{-1} (0.125–1.25 C; A C-rate is a measure of the rate at which a battery is discharged relative to its maximum capacity; for example 1C rate means that the discharge current will discharge the entire battery in 1 h). Over this range, the capacity of the Cu-substituted Co_3O_4 electrode exceeds 400 mA h g^{-1} , whereas for the control it drops below 100 mA h g^{-1} at the highest cycling rate. Likewise, such an improved electrochemical property has been

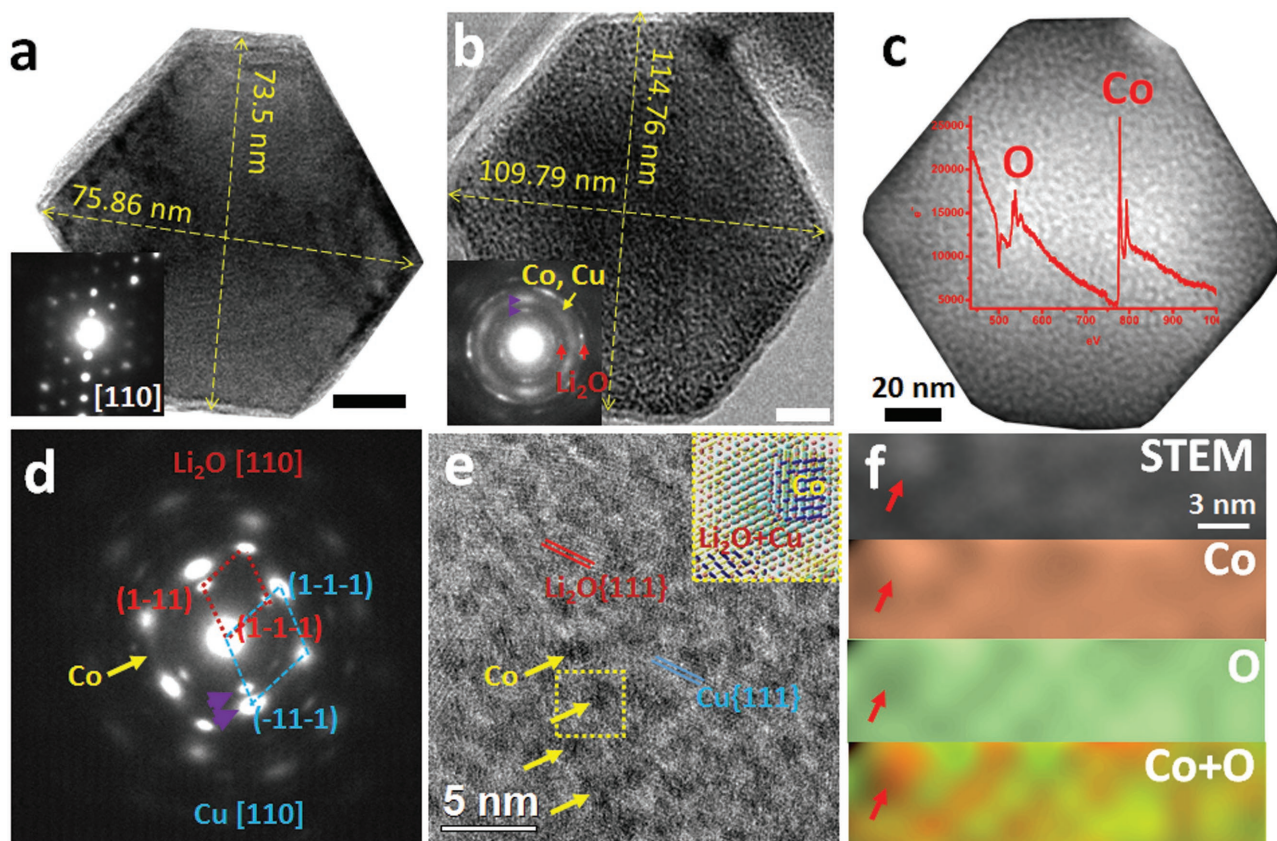


Figure 2. Lithiation of Cu-substituted Co_3O_4 studied by in situ TEM. a) A pristine, single-crystal Cu-substituted Co_3O_4 nanoparticle with hexagonal shape oriented closed to the $[110]$ zone axis (the diffraction pattern is shown as an inset). b) The nanoparticle after lithiation shows polycrystalline morphology consisting of Li_2O , metal Cu, and Co as determined by the inset electron diffraction. c) A Z-contrast STEM image of the lithiated nanoparticle, with an EELS spectrum as an inset showing both O and Co edges. d) Nanobeam electron diffraction of the lithiated Cu-substituted Co_3O_4 showing single-crystal like diffraction spots of Li_2O and Cu, and diffuse arcs of Co. The Cu $\{111\}$ lattice plane is parallel to the $\{111\}$ of Li_2O , as indicated by two purple arrowheads. e) HREM image of the lithiated Cu-substituted Co_3O_4 showing large Cu and Li_2O crystals on which small Co nanoparticles are formed, as illustrated by the inset. f) EELS maps of Co, O, and Co+O along with its Z-contrast STEM image of the lithiated Cu-substituted Co_3O_4 , confirming that the white dots are from Co-nanoparticle.

observed in other binary transition metal oxides,^[12] although the mechanism leading to such an improvement remains largely unknown.

To probe the physical mechanism that underlies the improved electrochemical performance of Cu-substituted Co_3O_4 , the lithiation of Cu-substituted Co_3O_4 was directly investigated by in situ transmission electron microscopy (TEM) (Figures S4 and S5, Video S1, Supporting Information) with a preassembled half-cell miniature battery configuration as illustrated in Figure S4a (Supporting Information). A representative pristine, single-crystalline Cu-substituted Co_3O_4 nanoparticle (Figure 2a) oriented close to the $[110]$ axis was chosen for examination during lithiation. The lithiation of this nanoparticle resulted in the formation of nanoscale crystallites (Figure 2b) with overall areal expansion of about 200% (Figures S4 and S5, Supporting Information), showing large volume expansion. In the selected area electron diffraction (SAED) pattern, shown as an inset in Figure 2b, diffraction rings of Li_2O and broader diffuse scattering can be observed, indicating that reaction product is a mixture of Li_2O , Cu, and Co nanocrystals (Figure S6, Supporting Information).

The orientation relationship between the formed Cu and Li_2O is further disclosed by nanobeam electron diffraction. Several bright diffraction spot arcs are observed along the diffuse rings, close to bright spots of Li_2O , as indicated by the purple arrowheads in Figure 2b. In the nanobeam electron diffraction pattern (Figure 2d), alignment of the diffraction spots is evident, as indicated by purple arrowheads in Figure 2d. These spots represent the Cu $\{111\}$ and Li_2O $\{111\}$ planes, while both crystals are oriented along the $[110]$ direction. In the pattern (Figure 2d), the Cu $_{(-11-1)}$ spot and Li_2O $_{(-11-1)}$ spot are not superimposed due to large mismatch ($\approx 22\%$). However, the two spots are in the same radial line without any rotational mismatch. Such an intimate relationship can also be observed for other diffraction spots, which demonstrates a cube-on-cube orientation relationship although the interface between Cu and Li_2O is incoherent. Both Cu and Li_2O show strong single-crystalline sharp spots, indicating that the crystalline size of Cu and Li_2O crystals is sufficiently large, in the range ≈ 20 nm (the beam size used for nanobeam diffraction was ≈ 50 nm) or larger. Meanwhile, the size of the Co clusters is very small, ≈ 2 nm, as measured from the high-resolution electron

microscopy (HREM) image. In addition, the Co clusters are likely defective and highly strained (Figure 2e and Figure S7, Supporting Information) as indicated by the broad diffuse arcs in the nanobeam diffraction pattern (Figure 2d). Moreover, the Co clusters appear as bright regions in the Z-contrast scanning TEM (STEM) image shown in Figure 2c. Combined with electron energy loss spectroscopy (EELS) of O and Co as shown as an inset in Figure 2c, the Co and O distribution can be spatially revealed (Figure 2f), confirming that the bright clusters in the STEM image are rich in Co.

At the end of the first lithiation, there are ≈ 2 nm Co clusters distributed on the ≈ 20 nm metal Cu and Li_2O crystals, with the Cu and Li_2O crystals exhibiting a cube-on-cube orientation relationship ($[100]//[100]$ and $(100)//(100)$), as illustrated as an inset in Figure 2e. We have also investigated the cycled Cu-substituted Co_3O_4 that was taken out from the coin cells after running at different cycles. The ex situ results obtained at the first and 10th cycle by ex situ observation (Figures S8 and S9, Supporting Information) agree well with the in situ TEM observations. In short, very fine Co-metal nanoclusters uniformly distributed on Cu and Li_2O crystals are formed at the end of the first lithiation, while Cu and Li_2O have the cube-on-cube orientation relationship although their lattice mismatch is large.

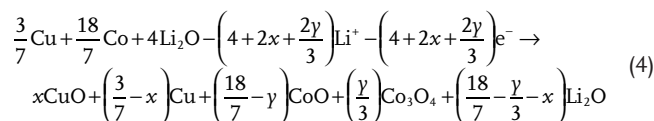
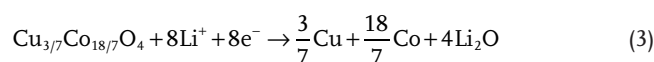
The Cu-substituted Co_3O_4 lithiation is further investigated at high resolution and in conjunction with density functional theory (DFT) simulations, to understand why Li_2O and Cu crystals have such an intimate and low-index cube-on-cube orientation relationship despite a large lattice mismatch. As shown in Figure 3a–d, Figure S10 and Videos S2–S4 (Supporting Information), the lithiation propagates with the motion of the interface delineating the lithiated and pristine phases. A closer observation of the interface (Figure 3e–g and Video S5, Supporting Information) reveals the formation of Li intercalated and crystalline phases with a notably expanded $\{022\}$ lattice spacing, from 0.28 ± 0.1 nm of the $\text{Cu}_{3/7}\text{Co}_{18/7}\text{O}_4$ to 0.30 ± 0.1 nm (Figure 3f) and 0.32 ± 0.1 nm (Figure 3g). However, further lithiation leads to phase separation, resulting in the formation of Li_2O and Cu crystals as evidenced by the splitting of spots in the Fourier transformation shown as an inset in Figure 3h. The Co atoms are extruded from the nanostructures forming Co clusters as marked by red arrows with the Co clusters growing larger as more lithium is inserted (Figure 3e–h). Instead of forming large ≈ 20 nm Cu crystals, Co atoms tend to form small clusters ≈ 2 nm when they are extruded.

The lithiation of Cu-substituted Co_3O_4 has been simulated (Figures S11–S13, Supporting Information) using DFT based nonequilibrium phase searching method,^[13] which shows the prediction of several intermediate and metastable phases. For the simplicity of supercell generation in DFT calculations and computational efficiency, the Cu/Co ratio is taken as 1:5 for the original phase before lithiation. From the $\{220\}$ spacing (referring to the spinel lattice), three intermediate phases predicted by DFT calculations are illustrated in Figure 3i–l, prior to the final phase separation by the conversion reaction (Figure 3m). Instead of direct transition from Cu-substituted Co_3O_4 to metal Cu, Co and Li_2O , the intermediate and Li-intercalated $\text{Li}_x\text{Cu}_{3/7}\text{Co}_{18/7}\text{O}_4$ phases provide a gradual transformation pathway to the formation of nanoscale Li_2O and Cu, allowing them to have a close orientation relationship. This explains

the experimentally observed orientation between these phases, even though they have large lattice mismatch. The reactions involved in Cu-substituted Co_3O_4 lithiation calculated by DFT are summarized in Table S1 (Supporting Information).

In the charging cycle (delithiation), the particles being charged maintain their shape and continue to have a polycrystalline structure as shown in Figure 4a and Figure S14 (Supporting Information). An unusual intimate orientation relationship between the formed CuO crystals and Cu has been disclosed while Cu is oxidized into CuO. In the SAED pattern of the delithiated sample (Figure 4b), several diffraction rings can be identified as CoO nanocrystals. The bright diffraction spots from larger crystals can be indexed as metal Cu and CuO, as shown in Figure 4c. After delithiation, there are ≈ 2 nm CoO clusters on the metal Cu and CuO crystals of ≈ 20 nm (Figure 4d), while Cu and the newly formed CuO crystals have a cubic-to-cubic orientation relationship (if one considers CuO as the pseudocubic lattice). The chemical state of both Cu and Co was identified by X-ray photoelectron spectroscopy (XPS) (Figure 4e), showing the oxidation of Co and partial oxidation of Cu during delithiation. Along with the decomposition of Li_2O , delithiation results in the Co nanoparticles being oxidized to CoO (and perhaps even $\text{Cu}_x\text{Co}_{3-x}\text{O}_4$). However, only some portion of the Cu metal is oxidized to CuO, as there is still clear metallic face centered cubic (fcc) Cu peaks in the electron diffraction. By simply assuming kinematic scattering and using the intensities of the Cu(111) and CuO(110) spots, the CuO/Cu atomic ratio is estimated to be about 4.7/1, which means in the delithiation about 20% of the Cu remains as support. The reactions during delithiation are summarized in Table S1 calculated by DFT. CuO has higher voltages (≈ 2.1 V) than that of CoO (≈ 1.7 V), meaning that metal Co will be oxidized first while Cu is still in the metallic form. Although it is not observed in the diffraction patterns, the presence of Co_3O_4 cannot be excluded since the voltage reaches more than 2.5 V.^[14]

The lithiation and delithiation reactions in the first cycle can be described as



where x is ratio of CuO/Cu to measure how much Cu has been oxidized and y is ratio of $\text{Co}_3\text{O}_4/\text{CoO}$ to measure how much Co^0 has been oxidized to Co^{3+} .

Part of the Li_2O formed in the first lithiation becomes inactive in the following cycles depending on how much Cu has been oxidized, which may partially contribute to the large capacity loss in the first cycle (besides the formation of solid electrolyte interphase (SEI)). In the subsequent cycles, although the Cu/CuO redox reaction tends to become more stable, the fluctuation of the amount of Cu being oxidized may eventually influence the actual capacity. This effect may explain why sometimes there is an increase in capacity, as is commonly observed in oxide electrodes.

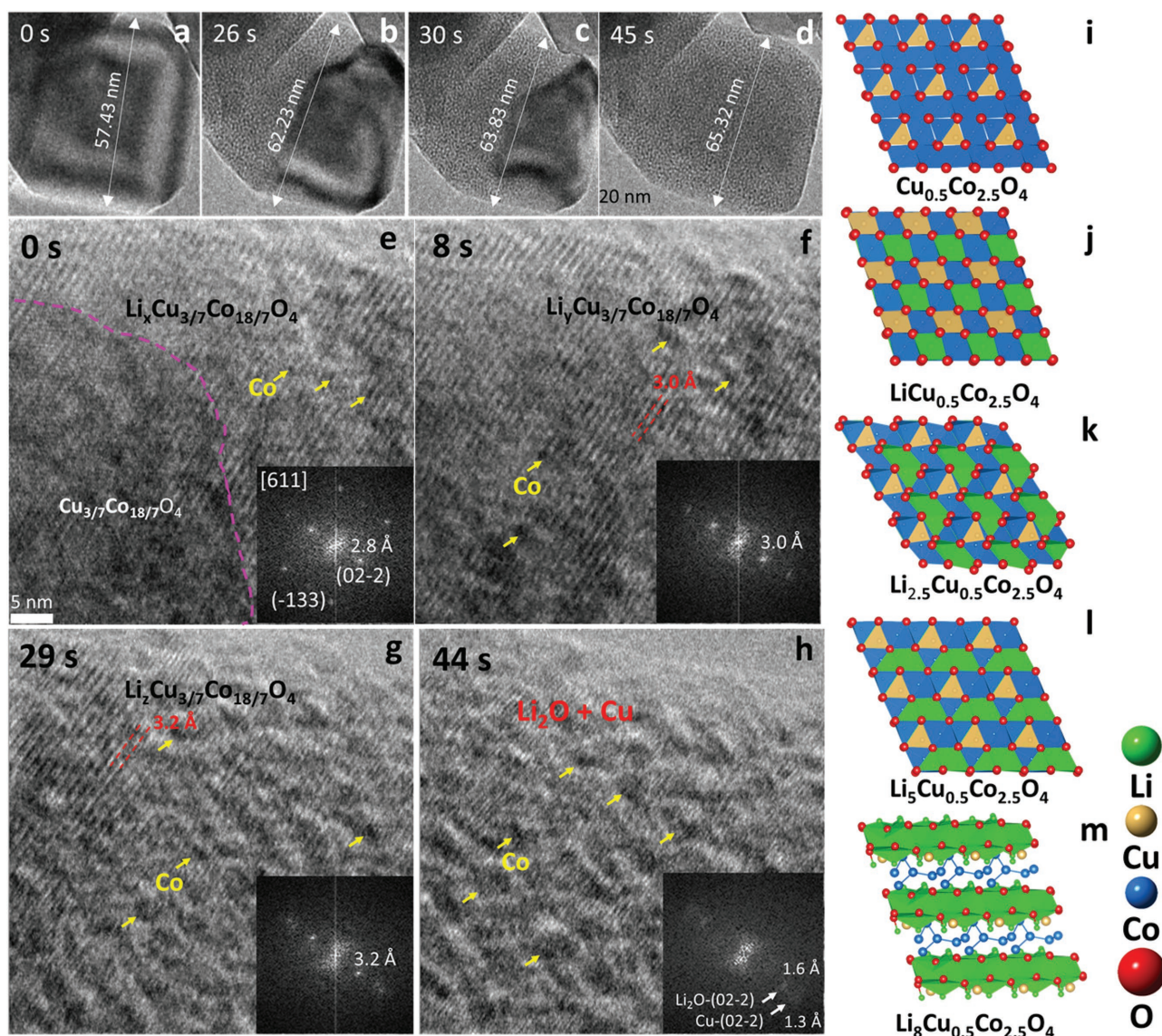


Figure 3. In situ HREM of the reaction front of Cu-substituted Co_3O_4 lithiation. a–d) In situ TEM images show the movement of the reaction front along with volumetric expansion. e–f) In situ HREM images of the reaction interface showing the formation of intermediate and intercalated phases and the formation of large Li_2O and Cu crystals and Co-nanoparticles at the few nanometer scale. The $\{220\}$ lattice spacing can be identified by Fourier transformation as shown as insets. i–m) Illustration of the intermediate and intercalated phases during lithiation of Cu-substituted Co_3O_4 using the Cu:Co ratio as 1:5 for the simplicity of supercell generation in DFT calculations.

The nanocomposites of small CoO nanoparticles uniformly distributed on a thin and stretchable metal Cu/CuO network appear robust for long duration cycling. In lithiation, Cu/CuO nanoplates and Cu/CoO interfaces provide enough sites for Li_2O nucleation and growth (illustrated in Figure 4k), which enables volumetric expansion without fracture. In delithiation, the intimate contact of Cu nanoplates and Co nanoparticles may act as a catalyst for the Li_2O decomposition reaction (illustrated in Figure 4l). In addition, the metal Cu nanoplates form a percolating network, enabling high electronic conductivity (Figure S15, Supporting Information). The two major products in lithiation, Cu (fcc with $a = 3.615 \text{ \AA}$) and Li_2O (fcc with $a = 4.619 \text{ \AA}$), have a simple cube-on-cube relationship, although their misfit is about 22%. In delithiation,

Cu and CuO (pseudocubic structure with $a = 4.778 \text{ \AA}$) have also a cube-on-cube relationship although their misfit is about 24%. The cube-on-cube relationship helps not only maintain the intimate contact between Li_2O and Cu in lithiation, and between CuO and Cu in delithiation, but also provide an efficient way of accommodating the Li_2O in lithiation and CuO in delithiation. Such an electrochemically driven confinement at nanoscale prompts the reversibility of the lithiation/delithiation reactions and thus the cycling stability. Among all the advantages brought by Cu substitution, the formation of Cu support is the most salient one. In pure Co_3O_4 without Cu substitution, Co nanoparticles formed in lithiation are on the nonconductive Li_2O support and may pulverize, and be lost in the following cycles when Li_2O decomposes in delithiation. In Cu-substituted

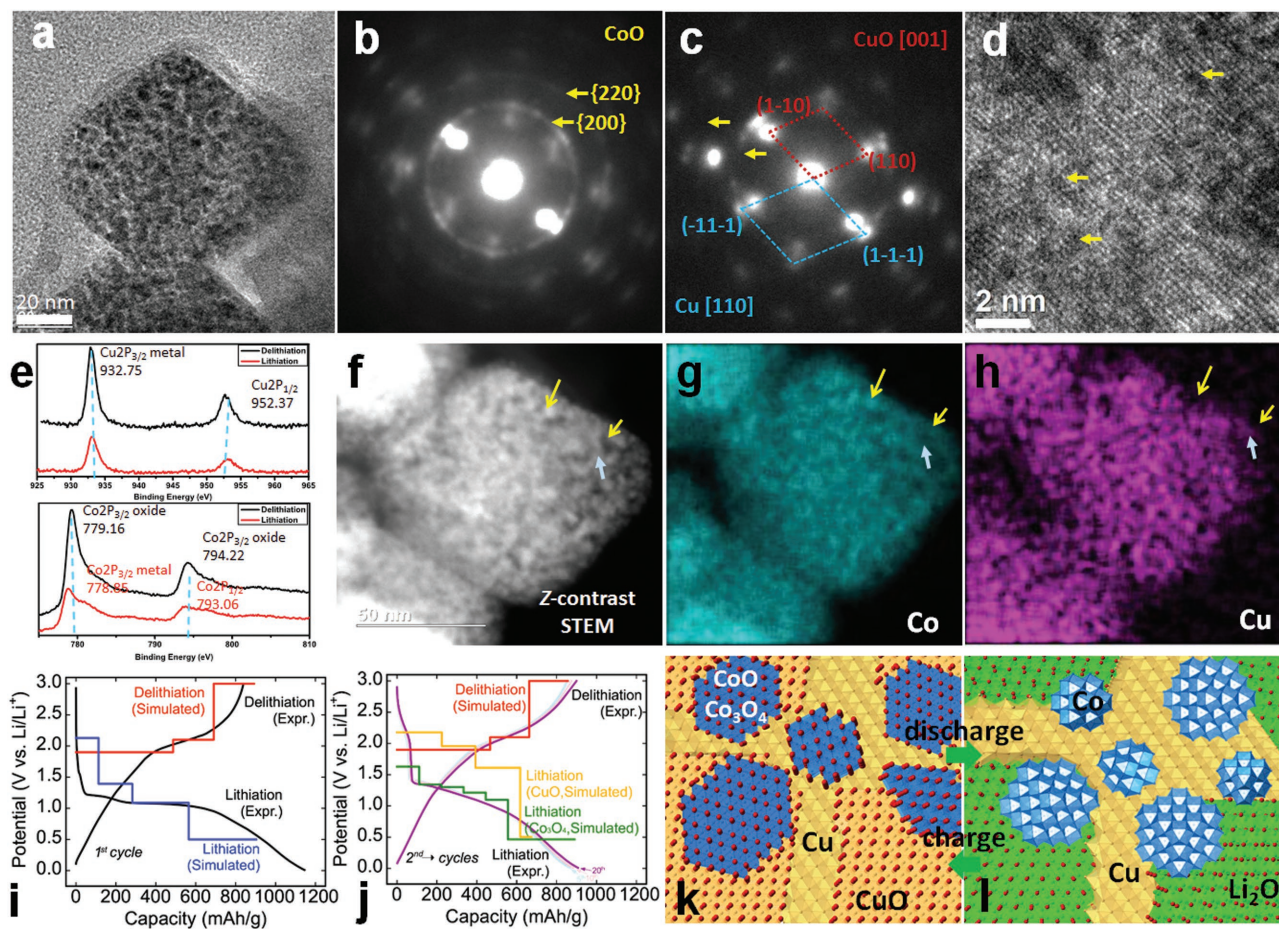


Figure 4. Structural evolution during Cu-substituted Co_3O_4 delithiation. a) A TEM image of the delithiated Cu-substituted Co_3O_4 showing that the rhombohedral shape with straight facets is well kept after delithiation. b) SAED pattern of the delithiated particle showing CoO diffraction rings along with some sharp spots from large crystals. c) Nanobeam electron diffraction pattern showing that the large spots are from Cu and CuO crystals. In situ TEM images show the movement of the reaction front along with volumetric expansion. d) HREM images of the delithiated sample showing CoO nanoparticles on the substrate of Cu and CuO . e) XPS spectra of lithiated and delithiated Cu-substituted Co_3O_4 samples showing Cu and Co peaks. The oxidation of Co and partial oxidation of Cu in delithiation are confirmed. f) Z-contrast STEM image, g) Co map, and h) Cu map of the delithiated sample. CoO clusters appear as bright spot in the STEM images. i) Comparison of experimental and DFT simulated voltage profiles for the first cycle of lithiation and delithiation. (j) Comparison of experimental and DFT simulated voltage profiles for the following cycles of lithiation and delithiation. k, l) Illustration of reversible structural changes in the charge and discharge cycles.

Co_3O_4 , large size Cu formed in lithiation serves as a high conductivity backbone and cohesive support to accommodate Co nanoclusters thus preventing active materials from losing mechanical integrity or electrical contact to the current collector. Meanwhile, the size of Co (in lithiation) and CoO (in delithiation) remains small due to the existence of the Cu which is immiscible with Co .

The lithiation reactions show an initial intercalation of lithium, prior to the conversion reaction.^[15] The intermediate phases formed during the nonequilibrium intercalation are not observed in delithiation and are likely not part of the ground-state equilibrium reactions. To explore the interplay among nonequilibrium, intercalation, and conversion reactions, we have developed a computational nonequilibrium phase search method to identify intermediate phases (Figures S11–S13, Supporting Information). The calculated voltage profiles (Figure 4i, j) based on the lithiation/delithiation reactions (listed in Table S1,

Supporting Information) fit well to the experimental curves. The lithiation and delithiation processes proceed through nonequilibrium and equilibrium reaction paths, respectively. Such a difference in reaction path has a contribution to the experimentally observed voltage hysteresis.

In conclusion, the substitution of a third metallic element (Cu) into binary oxides (Co_3O_4) alters the fundamental processes of lithiation/delithiation. Metal Cu intrinsically formed in the first lithiation cycle remains partially stable as a metallic support on which $\text{Li}_2\text{O} + \text{Co}/\text{CoO}$ redox products are anchored. The Cu -based network also provides a highly conductive pathway for electrons and enables Li -ion transport. Cu and Co are immiscible which prevents the aggregation of metal clusters, leaving enough space for Li_2O nucleation and growth. In addition, an unusual intimate orientation relationship between the Cu crystals and Li_2O crystal has been identified, and small Co/CoO clusters are found to remain active on the $\text{Cu}/\text{CuO}/\text{Li}_2\text{O}$

substrate in subsequent cycles. This “adaptive architecture” accommodates the formation of Li_2O in the discharge cycle and underpins the catalytic activity of Li_2O decomposition in the charging cycle. With proper design, these ternary oxides may be extended and applied to other electrochemical storage technologies, such as $\text{Li-Li}_2\text{O/Li}_2\text{O}_2$ batteries.

Experimental Section

Materials: Hydrothermal method was used to synthesize Cu-substituted Co_3O_4 nanocrystals. In a typical synthesis, 0.02 mmol $\text{Co}(\text{acac})_2$ and 0.02 mmol $\text{Cu}(\text{acac})_2 \cdot 2\text{H}_2\text{O}$ was dissolved in 10 mL deionized water and stirred for 1 h. Then 10 mL Co^{2+} (0.02 M) aqueous solution, 10 mL Cu^{2+} aqueous solution, and 10 mL 0.04 M NaF aqueous solution were mixed and stirred for 1 h. The mixed suspension was transferred into a 50 mL Teflon-lined stainless steel autoclave and kept at 160 °C for 12 h. The black precipitates in the bottom were collected and washed by centrifugation for three or four times (4500 rpm, 5 min) using ethanol. The power was dried at 80 °C for 12 h for the subsequent characterization and electrochemical measurements.

Characterization: Filed emission scanning electron microscope (Hitachi, SU-8030) was used to observe the microstructure of the prepared samples. Crystal structure was identified using X-ray diffraction with Cu-K α radiation (Scintag XDS2000). Field emission high-resolution transmission electron microscope (JEOL, JEM-2100F) and a dedicated STEM (Hitachi-2300) were employed to do the characterization.

Electrochemical Measurements: Active materials of Cu-substituted Co_3O_4 or Co_3O_4 were mixed with super-P carbon black and polyvinylidene fluoride at weight ratio of 70:20:10 using N-methyl-2-pyrrolidone as solvent. The obtained slurry was then coated on tailed Cu foil and dried at 80 °C for 12 h in a vacuum oven to remove the solvent and used as the working electrodes. Half-cells were assembled in Ar-filled glove box using pure lithium metal foil as the counterelectrode and Celgard 2325 membrane as separator. The 1M LiPF_6 in a mixture of ethylene carbonate and dimethyl carbonate (volume ratio = 1:1) was used as electrolyte.

The discharge and charge measurements of the half-cells were performed on a multichannel battery testing system Arbin BT-2143 between the volt range from 0.01 to 3 V (vs Li/Li^+) at room temperature. The rate performance of Cu-substituted Co_3O_4 and Co_3O_4 was also evaluated at different current densities from 0.1 to 1.0 A g^{-1} .

In Situ TEM: Like other windowless in situ TEM settings,^[8] the open half-cell was constructed in an in situ electrical probing TEM holder (Nanofactory Instrument). This holder had a dual-probe design, i.e., one Au rod was used as the sample holder with a small amount of Cu-substituted Co_3O_4 attached to its tip; on the other side an scanning tunneling microscope (STM) tungsten (W) probe driven by piezomotor capable of 3D positioning with a step size of 1 nm was used to mount Li metal (as shown in Figure S4a, Supporting Information). The W probe tip was scratched by Li metal strip and then affixed on the TEM holder inside an Ar-filled glove box. With an airtight cover, the TEM holder was transferred to TEM column with limited exposure to air (5 s), where a layer of lithium oxide was grown on the surface of Li metal and acted as a solid electrolyte for the nanocell Li-ion batteries.

First-Principle Calculations: All the first-principle calculations were conducted via the Vienna Ab initio Simulation Package^[16] with the projector augmented wave potentials.^[17] For the exchange-correlation functional, we used the generalized gradient approximation of Perdew–Becke–Ernzerhof^[18] with spin polarization considered. We used two different sets of parameters: one for lower energy configuration sampling and the other for accurate total energy determination of these lower energy configurations determined. For the coarse energy sampling calculations, a plane-wave basis set with a cutoff energy of 300 eV and Γ -centered k-meshes with the density of 2000 k-points per reciprocal atom were used. The accurate total energy calculations were performed with a plane-wave basis set cutoff energy of 520 eV and Γ -centered k-meshes with the density of 8000 k-points per reciprocal atom. DFT + U

method^[19] was used to treat the 3d electrons of Co and Cu ions with U values of 3.3 and 4.0 eV adopted following previous studies.^[19,20]

Supporting Information

Supporting Information is available from the Wiley Online Library or from the author.

Acknowledgements

H.L. and Q.L. contributed equally to this work. Q.L. and J.W. (in situ TEM and interpretation), Z.Y. and C.W. (DFT calculation), L.L. and M.H. (battery measurements), and V.P.D. (TEM interpretation) were supported as part of the Center for Electrochemical Energy Science, an Energy Frontier Research Center funded by the U.S. Department of Energy (DOE), Office of Science, Basic Energy Sciences under Award # DEAC02-06CH11357. Q.L., J.W., and V.P.D. were also supported by the Samsung Advanced Institute of Technology (SAIT)’s Global Research Outreach (GRO) Program and the Initiative for Sustainability and Energy at Northwestern (ISEN). Portions of this work were performed in the NUANCE Center at Northwestern University, using the EPIC facility that receives support from the Soft and Hybrid Nanotechnology Experimental (SHyNE) Resource (NSF NNCI-1542205); the MRSEC program (NSF DMR-1720139) at the Materials Research Center; the International Institute for Nanotechnology (IIN); the Keck Foundation; and the State of Illinois, through the IIN. The authors gratefully acknowledge computing resources from: (1) the National Energy Research Scientific Computing Center, a DOE Office of Science User Facility supported by the Office of Science of the U.S. Department of Energy under Contract DE-AC02-05CH11231; (2) Blues, a high-performance computing cluster operated by the Laboratory Computing Resource Center at Argonne National Laboratory.

Conflict of Interest

The authors declare no conflict of interest.

Keywords

Cu-doping transition metal oxides, cycling stability, in situ transmission electron microscopy (TEM), lithium-ion batteries

Received: August 24, 2017

Revised: September 29, 2017

Published online: December 6, 2017

- [1] E. Peled, C. Menachem, D. Bar-Tow, A. Melman, *J. Electrochem. Soc.* **1996**, *143*, L4.
- [2] K.-S. Chen, R. Xu, N. S. Luu, E. B. Secor, K. Hamamoto, Q. Li, S. Kim, V. K. Sangwan, I. Balla, L. M. Guiney, *Nano Lett.* **2017**, *17*, 2539.
- [3] K. Mizushima, P. Jones, P. Wiseman, J. B. Goodenough, *Mater. Res. Bull.* **1980**, *15*, 783.
- [4] a) P. Poizot, S. Laruelle, S. Grugeon, L. Dupont, J. Tarascon, *Nature* **2000**, *407*, 496; b) P.-L. Taberna, S. Mitra, P. Poizot, P. Simon, J.-M. Tarascon, *Nat. Mater.* **2006**, *5*, 567.
- [5] a) B. Boukamp, G. Lesh, R. Huggins, *J. Electrochem. Soc.* **1981**, *128*, 725; b) M. Obrovac, L. Christensen, *Electrochem. Solid-State Lett.* **2004**, *7*, A93; c) H. Wu, Y. Cui, *Nano Today* **2012**, *7*, 414.

- [6] H. Wang, Y. Yang, Y. Liang, J. T. Robinson, Y. Li, A. Jackson, Y. Cui, H. Dai, *Nano Lett.* **2011**, *11*, 2644.
- [7] a) Q. Li, H. Liu, Z. Yao, J. Cheng, T. Li, Y. Li, C. Wolverton, J. Wu, V. P. Dravid, *ACS Nano* **2016**, *10*, 8788; b) A. Abouimrane, D. Dambournet, K. W. Chapman, P. J. Chupas, W. Weng, K. Amine, *J. Am. Chem. Soc.* **2012**, *134*, 4505; c) Y. Cui, A. Abouimrane, J. Lu, T. Bolin, Y. Ren, W. Weng, C. Sun, V. A. Maroni, S. M. Heald, K. Amine, *J. Am. Chem. Soc.* **2013**, *135*, 8047.
- [8] a) M. T. McDowell, S. W. Lee, J. T. Harris, B. A. Korgel, C. Wang, W. D. Nix, Y. Cui, *Nano Lett.* **2013**, *13*, 758; b) Q. Li, J. Wu, J. Xu, V. P. Dravid, *J. Mater. Chem. A* **2016**, *4*, 8669; c) J. Y. Huang, L. Zhong, C. M. Wang, J. P. Sullivan, W. Xu, L. Q. Zhang, S. X. Mao, N. S. Hudak, X. H. Liu, A. Subramanian, *Science* **2010**, *330*, 1515; d) X. H. Liu, J. Y. Huang, *Energy Environ. Sci.* **2011**, *4*, 3844; e) X. H. Liu, J. W. Wang, S. Huang, F. Fan, X. Huang, Y. Liu, S. Krylyuk, J. Yoo, S. A. Dayeh, A. V. Davydov, *Nat. Nanotechnol.* **2012**, *7*, 749; f) Q. Su, L. Chang, J. Zhang, G. H. Du, B. S. Xu, *J. Phys. Chem. C* **2013**, *117*, 4292; g) L. Luo, J. S. Wu, J. M. Xu, V. P. Dravid, *ACS Nano* **2014**, *8*, 11560; h) Y. Yuan, K. Amine, J. Lu, R. Shahbazian-Yassar, *Nat. Commun.* **2017**, *8*, 15806.
- [9] a) F. Wang, H.-C. Yu, M.-H. Chen, L. Wu, N. Pereira, K. Thornton, A. Van der Ven, Y. Zhu, G. G. Amatucci, J. Graetz, *Nat. Commun.* **2012**, *3*, 1201; b) F. Jiang, Q. Su, H. Li, L. Yao, H. Deng, G. Du, *Chem. Eng. J.* **2017**, *314*, 301; c) S. Liu, S. Zhang, Y. Xing, S. Wang, R. Lin, X. Wei, L. He, *Electrochim. Acta* **2014**, *150*, 75; d) Y. Sharma, N. Sharma, G. V. S. Rao, B. V. R. Chowdari, *J. Power Sources* **2007**, *173*, 495; e) S. G. Mohamed, Y.-Q. Tsai, C.-J. Chen, Y.-T. Tsai, T.-F. Hung, W.-S. Chang, R.-S. Liu, *ACS Appl. Mater. Interfaces* **2015**, *7*, 12038; f) Y. Liu, L.-J. Cao, C.-W. Cao, M. Wang, K.-L. Leung, S.-S. Zeng, T. Hung, C. Chung, Z.-G. Lu, *Chem. Commun.* **2014**, *50*, 14635; g) Q. Li, L. Yin, Z. Q. Li, X. K. Wang, Y. X. Qi, J. Y. Ma, *ACS Appl. Mater. Interfaces* **2013**, *5*, 10975.
- [10] H. Li, P. Balaya, J. Maier, *J. Electrochem. Soc.* **2004**, *151*, A1878.
- [11] Z.-S. Wu, W. Ren, L. Wen, L. Gao, J. Zhao, Z. Chen, G. Zhou, F. Li, H.-M. Cheng, *ACS Nano* **2010**, *4*, 3187.
- [12] a) R. Alcántara, M. Jaraba, P. Lavela, J. Tirado, *Chem. Mater.* **2002**, *14*, 2847; b) R. Ning, J. Tian, A. M. Asiri, A. H. Qusti, A. O. Al-Youbi, X. Sun, *Langmuir* **2013**, *29*, 13146; c) W. Kang, Y. Tang, W. Li, Z. Li, X. Yang, J. Xu, C.-S. Lee, *Nanoscale* **2014**, *6*, 6551; d) L. Shen, L. Yu, X. Y. Yu, X. Zhang, X. W. D. Lou, *Angew. Chem., Int. Ed.* **2015**, *54*, 1868; e) B. Liu, J. Zhang, X. Wang, G. Chen, D. Chen, C. Zhou, G. Shen, *Nano Lett.* **2012**, *12*, 3005.
- [13] a) Q. Li, Z. Yao, J. Wu, S. Mitra, S. Hao, T. S. Sahu, Y. Li, C. Wolverton, V. P. Dravid, *Nano Energy* **2017**, *38*, 342; b) Z. Yao, S. Kim, M. Aykol, Q. Li, J. Wu, J. He, C. Wolverton, *Chem. Mater.* **2017**, <https://doi.org/abs/10.1021/acs.chemmater.7b02058>; c) K. He, Z. Yao, S. Hwang, N. Li, K. Sun, H. Gan, Y. Du, H. Zhang, C. Wolverton, D. Su, *Nano Lett.* **2017**, *17*, 5726.
- [14] H. S. Jadhav, S. M. Pawar, A. H. Jadhav, G. M. Thorat, J. G. Seo, *Sci. Rep.* **2016**, *6*, 31120.
- [15] a) M. Thackeray, S. Baker, J. Coetzer, *Mater. Res. Bull.* **1982**, *17*, 405; b) M. Thackeray, S. Baker, K. Adendorff, J. Goodenough, *Solid State Ionics* **1985**, *17*, 175; c) D. Larcher, G. Sudant, J. Leriche, Y. Chabre, J. Tarascon, *J. Electrochem. Soc.* **2002**, *149*, A234; d) H. Hwang, H. Kim, J. Cho, *Nano Lett.* **2011**, *11*, 4826.
- [16] a) G. Kresse, J. Hafner, *Phys. Rev. B* **1993**, *47*, 558; b) G. Kresse, J. Hafner, *Phys. Rev. B* **1994**, *49*, 14251; c) G. Kresse, J. Furthmüller, *Comput. Mater. Sci.* **1996**, *6*, 15; d) G. Kresse, J. Furthmüller, *Phys. Rev. B* **1996**, *54*, 11169.
- [17] P. E. Blöchl, *Phys. Rev. B* **1994**, *50*, 17953.
- [18] J. P. Perdew, M. Ernzerhof, K. Burke, *J. Chem. Phys.* **1996**, *105*, 9982.
- [19] S. Dudarev, G. Botton, S. Savrasov, C. Humphreys, A. Sutton, *Phys. Rev. B* **1998**, *57*, 1505.
- [20] L. Wang, T. Maxisch, G. Ceder, *Phys. Rev. B* **2006**, *73*, 195107.